ACS Catalysis

Research Article

pubs.acs.org/acscatalysis

Zinc Promotion of Platinum for Catalytic Light Alkane Dehydrogenation: Insights into Geometric and Electronic Effects

Viktor J. Cybulskis,[†] Brandon C. Bukowski,[†] Han-Ting Tseng,[†] James R. Gallagher,[‡] Zhenwei Wu,[†] Evan Wegener,[†] A. Jeremy Kropf,[‡] Bruce Ravel,[§] Fabio H. Ribeiro,[†] Jeffrey Greeley,*[,†] and Jeffrey T. Miller*[,†]

[†]Davidson School of Chemical Engineering, Purdue University, 480 Stadium Mall Drive, West Lafayette, Indiana 47907, United States

[‡]Chemical Sciences and Engineering Division, Argonne National Laboratory, 9700 South Cass Avenue, Argonne, Illinois 60439, United States

[§]Materials Measurement Laboratory, National Institute of Standards and Technology, 100 Bureau Drive, M/S 8300, Gaithersburg, Maryland 20899, United States

Supporting Information

ABSTRACT: Supported metal nanoparticles are vital as heterogeneous catalysts in the chemical transformation of hydrocarbon resources. The catalytic properties of these materials are governed by the surface electronic structure and valence orbitals at the active metal site and can be selectively tuned with promoters or by alloying. Through an integrated approach using density functional theory (DFT), kinetics, and *in situ* X-ray spectroscopies, we demonstrate how Zn addition to Pt/SiO_2 forms high symmetry Pt_1Zn_1 nanoparticle alloys with isolated Pt surface sites that enable near 100% C_2H_4 selectivity during ethane dehydrogenation (EDH) with a 6-fold higher turnover rate (TOR) per mole of surface Pt at 600 °C compared to monometallic Pt/SiO_2. Furthermore, we show how DFT calculations accurately reproduce the resonant inelastic X-ray spectroscopic (RIXS) signatures of Pt 5d valence orbitals in the Pt/SiO_2 and $PtZn/SiO_2$ catalysts that correlate with their kinetic performance during EDH. This technique reveals that Zn modifies the energy of the Pt 5d electrons in PtZn, which directly relates to TOR promotion, while ensemble effects from the incorporation of Zn into the catalyst surface lead to enhanced product selectivity.

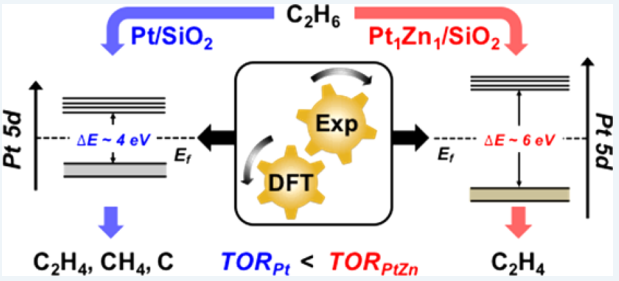

KEYWORDS: *dehydrogenation, heterogeneous catalysis, RIXS spectroscopy, density functional calculations, electronic structure, nanoparticles*

INTRODUCTION

The recent surge in gas production from shale formations throughout the United States presents a tremendous opportunity to develop catalytic innovations that efficiently transform hydrocarbon resources (i.e., methane, ethane, propane, butanes) directly into value-added chemicals and fuels with reduced environmental impact by selectively activating paraffinic C−H bonds.[1] Although various routes to synthesize alkene and aromatic building block molecules over metal-containing catalysts by dehydrogenation[2] and cyclization,[3] respectively, have been well-studied, fundamental understanding of issues regarding long-term catalyst stability, product selectivity, and turnover rates (TOR) still remain problematic.[4,5] Many of the challenges associated with developing new materials to overcome these limitations can only be addressed at the molecular level.

Noble metals, such as Pt, are well-known for exceptional performance in hydrocarbon catalysis, particularly for hydrogenation and isomerization reactions, due to their affinity for paraffinic C−H bonds.[2] Since the reactivity of metal nanoparticle surfaces is determined by the electronic states through the valence d bands, which is a region in the partial density of states (DOS),[6,7] one way we may alter the electronic structure of these surfaces, and hence, their reactivity, is by alloying of the surface with various promoters that can influence the availability and energies of the valence electrons to form chemical bonds with adsorbates. For example, the addition of Zn or Sn to Pt-containing catalysts has led to improved alkene selectivity during alkane dehydrogenation.[8−10] It has been suggested that these ad-metals modify the electronic properties of the noble metal sites by donating electron density and weakening the adsorption of π-bonded alkenes; thus, inhibiting the formation of coke precursors.[10−13] Yet, the energy levels of the d states of Pt and Pt-containing alloys, which also direct bond formation, have seldom been directly measured experimentally.

Received: December 19, 2016
Revised: May 8, 2017
Published: May 11, 2017

DOI: 10.1021/acscatal.6b03603
ACS Catal. 2017, 7, 4173−4181

While structure-insensitive reactions, such as alkene hydrogenation and alkane dehydrogenation, can occur on isolated Pt sites, it has been shown that larger Pt ensembles catalyze structure-sensitive reactions, including cracking and hydrogenolysis.[14−18] Recent experimental work by Childers et al.[19] has also shown that Zn addition to supported Pd catalysts can enhance propylene selectivity during propane dehydrogenation (PDH). The improved catalyst stability is attributed to the formation of a PdZn alloy with isolated Pd surface sites that eliminate the structure-sensitive hydrogenolysis pathway.[20] Similar conclusions regarding the importance of active site isolation (i.e., geometric effects) have been reported for SiO_2-supported PdIn[21] and PtIn[22] intermetallic alloys during ethane dehydrogenation (EDH).

Experimentally, the electronic structure of metal nanoparticles on heterogeneous catalysts can be accessed by using L edge, resonant inelastic X-ray scattering (RIXS) to monitor the energy of the d-band filled and unfilled states.[23−25] As a hard X-ray, two-photon process, RIXS permits the elucidation of electron excitations between inner-shell and valence levels within a specific element under working reaction conditions, thus making it possible to directly probe the surface chemistry at metal active sites and map the entire d-band spectrum to identify electronic descriptors of catalytic activity. As shown for the Pt L_3 edge in Scheme 1, absorption of a photon with energy

Scheme 1. RIXS Energy Scheme for Pt 2p ↔ 5d Transitions

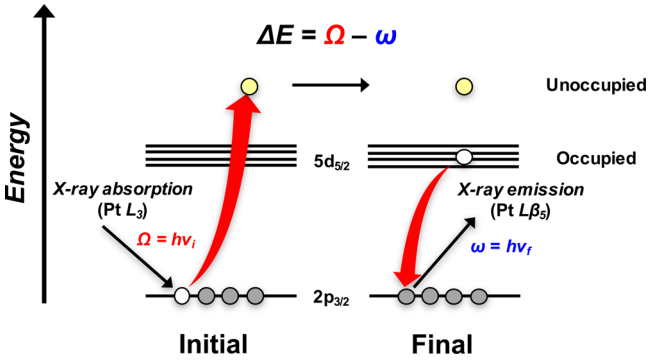

Ω promotes a 2p electron to an unoccupied state in the 5d valence shell and leaves behind a core hole that is subsequently refilled by an electron from filled orbitals. Filling of the core hole results in an emitted photon whose energy is dependent on the energy of the filled orbital. With a high-energy resolution spectrometer, the energy (ω) of the fluorescent photon from the filled 5d orbital can be determined (e.g., Pt $L\beta_5$ transition). The difference in energy between Ω and ω represents the overall energy transfer of the system (ΔE).

Many of the valence-to-core X-ray emission studies to date have been focused on the K edge (s → p) for inorganic and bioinorganic metal complexes to examine metal-to-ligand charge transfer as well as changes in bonding and antibonding states.[26] However, the K edge cannot access chemical information on the valence d electrons that are relevant for catalysis. While RIXS has successfully been applied at the L edge for 3d and 4d transition metal complexes to examine crystal field splitting and orbital occupancy,[27−29] there are relatively few studies on 5d metals,[24,30,31] such as Pt, that examine the electronic structure of supported noble metal nanoparticles.

Here, by using *in situ* X-ray absorption and synchrotron X-ray diffraction, we show that Pt_1Zn_1 intermetallic alloy nanoparticles are preferentially formed from Pt and Zn precursors on an amorphous SiO_2 support. These bimetallic alloy catalysts contain isolated surface Pt atoms with only metallic Zn nearest neighbors and display high ethylene selectivity (~100%) during EDH at 600 °C. We also show how the capabilities of RIXS analysis can provide a unique fingerprint for the catalytic properties of Pt/SiO_2 and $PtZn/SiO_2$ dehydrogenation catalysts. This spectroscopic characterization of metal nanoparticle electronic valence states can be coupled with kinetic measurements of catalytic performance to describe how Zn addition to Pt/SiO_2 modifies the metal nanoparticle electronic structure to affect the EDH TOR. Last, we suggest that DFT RIXS calculations for Pt-containing alloy compositions provide additional electronic structural information, thereby complementing and strengthening existing d-band models.

RESULTS AND DISCUSSION

Ethane Dehydrogenation on Pt/SiO_2 and $PtZn/SiO_2$. The Pt/SiO_2 and $PtZn/SiO_2$ catalysts for this study were prepared by pH-controlled incipient wetness impregnation (pH-IWI) of high-purity SiO_2 with $(NH_3)_4Pt(NO_3)_2$ and $Zn(NO_3)_2{\cdot}6H_2O$ precursors to obtain 9.70 wt % Pt for Pt/SiO_2 and 9.28 wt % Zn and 9.53 wt % Pt for $PtZn/SiO_2$. A high Pt

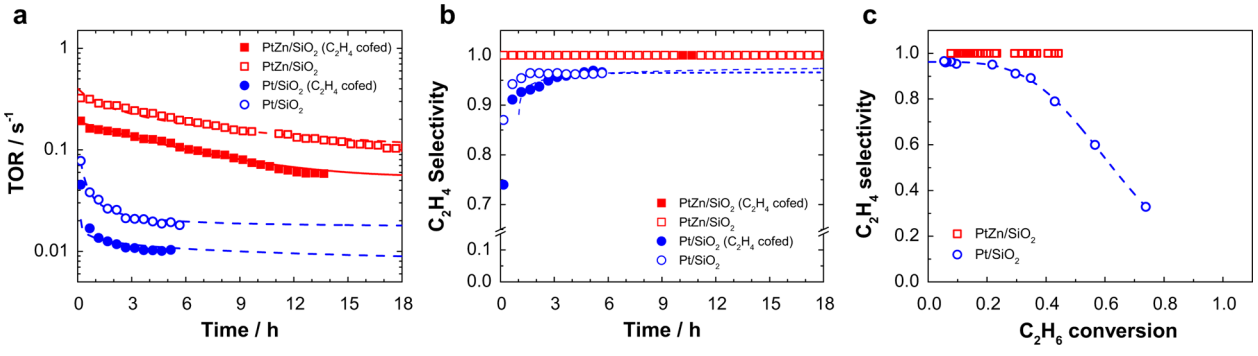

Figure 1. Ethane dehydrogenation kinetics for Pt/SiO_2 and $PtZn/SiO_2$. (a) TOR as a function of time on stream during EDH (2.5% C_2H_6, 1% H_2, 0.5% C_2H_4) at 600 °C on 9.70 wt % Pt/SiO_2 with C_2H_4 cofed (blue closed circles), 9.70 wt % Pt/SiO_2 without C_2H_4 cofed (blue open circles), 9.53 wt % Pt−9.28 wt % Zn/SiO_2 with C_2H_4 cofed (red closed squares), and 9.53 wt % Pt−9.28 wt % Zn/SiO_2 without C_2H_4 cofed (red open squares). (b) C_2H_4 selectivities as a function of time on stream during EDH at 600 °C. (c) C_2H_4 selectivities as a function of C_2H_6 conversion during EDH (2.5% C_2H_6, 1% H_2) at 600 °C for 9.70 wt % Pt/SiO_2 (blue open circles) and 9.53 wt % Pt−9.28 wt % Zn/SiO_2 (red open squares).

DOI: 10.1021/acscatal.6b03603
ACS Catal. 2017, 7, 4173−4181

loading was required in order to obtain sufficient signal-to-noise during *in situ* RIXS experiments due to the relatively weak intensity of the valence $5d_{5/2} \rightarrow 2p_{3/2}$ ($L\beta_5$) X-ray emission line for Pt. Pt dispersions based on the measured H_2 uptake (Table S1) on the freshly reduced Pt/SiO_2 and $PtZn/SiO_2$ catalysts were determined to be 27% and 44%, respectively. Catalyst testing was performed at 600 °C in a gas mixture of 2.5% C_2H_6, 1% H_2, and 0.5% C_2H_4 to achieve differential C_2H_6 conversion ($X < 0.1$) and allow the reaction rate to be treated as constant throughout the reactor (section 3, Supporting Information).

As shown in Figure 1a, the EDH TOR, normalized per surface Pt atom, for Pt/SiO_2 (blue closed circles) stabilized at 0.01 s^{-1} after 5 h on stream from a starting value of 0.05 s^{-1}. During this period, the C_2H_4 selectivity reached 96% (X = 0.09) from a starting value of 74% (X = 0.4) as shown in Figure 1b (blue closed circles). Following the catalyst stabilization, the apparent activation energy between 570 and 600 °C was determined to be 72 ± 4 kJ mol^{-1} (Figure S1). At the start of the run, the carbon mass balance closed at 83%, indicating significant coke deposition on the clean catalyst surface, and then ultimately reached 100% after the stabilization period. This result, along with observed CH_4 formation during the reaction, shows that C_2H_6 hydrogenolysis and C_2H_4 decomposition reactions occur concomitantly with dehydrogenation on Pt. For $PtZn/SiO_2$, the EDH TOR per surface Pt was a factor of 6 higher than on Pt/SiO_2, as indicated by the red closed squares in Figure 1a, and reached 0.06 s^{-1} after 12 h from a starting value of 0.2 s^{-1}. Throughout the stabilization period, the C_2H_4 selectivity (Figure 1b) and carbon mass balance both remained near 100% indicating that dehydrogenation occurs almost exclusively on PtZn. The measured apparent activation energy for $PtZn/SiO_2$ was 99 ± 5 kJ mol^{-1} (Figure S1) and is similar to the 102 kJ mol^{-1} result reported by Galvita et al.[17] for PtSn/Mg(Al)O. Metal cluster size distributions on the used Pt/SiO_2 and $PtZn/SiO_2$ samples after EDH at 600 °C were analyzed from HAADF-STEM and TEM images and determined to be 3.3 ± 1.9 nm and 2.5 ± 0.6 nm, respectively (Figures S2–S4).

When C_2H_4 was removed from the reaction feed stream (Figure 1a), the TOR for both Pt/SiO_2 (blue open circles) and $PtZn/SiO_2$ (red open squares) increased by a factor of 2, which indicates that C_2H_4 inhibits the EDH reaction by competing with C_2H_6 for Pt surface sites. As shown in Figure 1b, the C_2H_4 selectivities for both Pt/SiO_2 and $PtZn/SiO_2$ were comparable to EDH with C_2H_4 cofed in the reaction mixture. At low C_2H_6 conversion ($X < 0.1$), the C_2H_4 selectivity on Pt/SiO_2 was similar to $PtZn/SiO_2$ but decreased to less than 50% at conversions above the equilibrium limit for dehydrogenation (X_{eq} = 0.54) as concomitant C–C bond cleavage reactions became dominant (Figure 1c). Conversely, $PtZn/SiO_2$ was able to maintain near 100% selectivity to C_2H_4 up to the thermodynamically limited equilibrium conversion, indicating that the active Pt surface sites are able to suppress cracking and hydrogenolysis reactions, even with H_2 (produced during EDH) present in the reactor.

Geometric Structures of Pt and PtZn Nanoparticles. The Pt and PtZn nanoparticle structures were determined by using *in situ* X-ray absorption spectroscopy (XAS) and synchrotron X-ray diffraction (XRD). The X-ray absorption near edge structure (XANES) at the Pt L_3 edge (E = 11 564 eV) shows that the supported Pt nanoparticles on Pt/SiO_2 were metallic (Pt^0), as evidenced by the similar edge positons (defined as the inflection point of the leading edge, which is determined from the maximum of the first derivative of the experimental XANES spectrum) and white-line intensities between the Pt foil and the Pt/SiO_2 catalyst (Figure S5). The Pt atoms in $PtZn/SiO_2$ were also metallic, and the edge energy increased as a result of Zn addition by 0.9 eV compared to Pt/SiO_2. Although the shape of the Pt L_3 XANES for metallic nanoparticles below approximately 3 nm in diameter exhibits slight differences compared to that for Pt foil, the edge energy is not changed.[32] Thus, changes in the edge energy can only be attributed to the formation of bimetallic PtZn nanoparticles. The *in situ* extended X-ray absorption fine structure (EXAFS) spectrum (black open circles) and fit of the isolated first scattering shell for 9.70 wt % Pt/SiO_2 (blue dashed line) in the top half of Figure 2a revealed that the metallic Pt

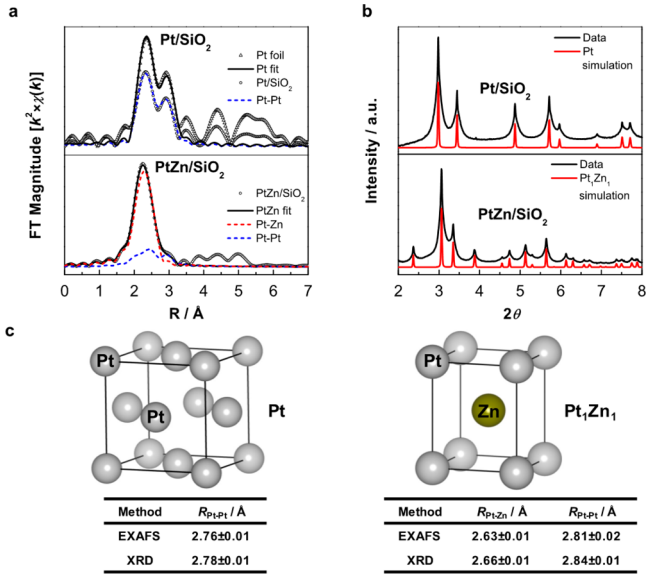

Method	R_{Pt-Pt} / Å
EXAFS	2.76±0.01
XRD	2.78±0.01

Method	R_{Pt-Zn} / Å	R_{Pt-Pt} / Å
EXAFS	2.63±0.01	2.81±0.02
XRD	2.66±0.01	2.84±0.01

Figure 2. Structural characterization of Pt and PtZn nanoparticles. (a) *In situ* EXAFS at the Pt L_3 edge and isolated first scattering shell fits for 9.70 wt % Pt/SiO_2 and 9.53 wt % Pt–9.28 wt % Zn/SiO_2 obtained at room temperature after H_2 reduction at 600 °C. (b) *In situ* XRD patterns obtained for 9.70 wt % Pt/SiO_2 and 9.53 wt % Pt–9.28 wt % Zn/SiO_2 at room temperature and compared to simulated patterns for Pt and Pt_1Zn_1, respectively. (c) Structures of Pt and Pt_1Zn_1 intermetallic alloy along with bond distances from *in situ* EXAFS simulation of *in situ* XRD patterns for 9.70 wt % Pt/SiO_2 and 9.53 wt % Pt–9.28 wt % Zn/SiO_2 at room temperature.

nanoparticles on Pt/SiO_2 are structurally similar to the bulk Pt foil (black open triangles) and that each Pt atom was surrounded by an average of 8.9 ± 0.9 Pt nearest neighbors at a bond distance of 2.76 ± 0.01 Å. On the basis of the metal dispersion correlation reported by Miller et al.,[33] the average Pt cluster size on Pt/SiO_2 was 4.2 ± 1.1 nm, consistent with the 3.3 ± 1.9 nm cluster size distribution from HAADF-STEM and TEM images of the used catalyst after EDH (Figures S2 and S4a).

For $PtZn/SiO_2$, each Pt atom was surrounded by an average of approximately seven Zn nearest neighbors (7.1 ± 0.6) at a bond distance of 2.62 ± 0.01 Å as shown by the first shell fit in the bottom half for Figure 2a (red dashed line). A Pt–Pt contribution was also fit in $PtZn/SiO_2$ with a coordination number of 3.6 ± 0.3 at an average bond distance of 2.81 ± 0.02 Å as shown by the first shell fit in the bottom half for Figure 2a (blue dashed line). This Pt–Pt distance is longer than that in

DOI: 10.1021/acscatal.6b03603
ACS Catal. 2017, 7, 4173–4181

monometallic Pt (i.e., at a nonbonding distance) and indicates that the Pt atoms in the PtZn nanoparticles were geometrically isolated from one another. Individual fitting parameters for the Pt foil, Pt/SiO_2, and $PtZn/SiO_2$ samples can be found in Table S2.

The synchrotron XRD pattern for Pt/SiO_2 at room temperature further confirms that the Pt nanoparticles were metallic, as indicated by the agreement between the peak positions of the simulated Pt metal pattern (red line) and the data (black line) in Figure 2b. The Pt/SiO_2 diffraction peaks were broadened due to the small (3.3 ± 1.9 nm by HAADF-STEM and TEM) nanoparticle size. In order to isolate these structural features, background scattering due to the SiO_2 support and empty heating stage were subtracted from the patterns for the Pt/SiO_2 and $PtZn/SiO_2$ catalysts according to the method described by Gallagher et al.[34] The background-subtracted patterns taken at 600 °C (Figure S6) were found to be identical to those obtained at room temperature (Figure 2b) except for shifts in diffraction peaks due to thermal lattice expansion, thereby indicating that the crystal structures of the Pt and PtZn nanoparticles remained unchanged throughout this temperature range. Thus, the diffraction patterns collected at room temperature were used for comparison with standard patterns simulated under the same conditions.

PtZn nanoparticles on the $PtZn/SiO_2$ sample (black line) in Figure 2b show diffraction peaks attributed to a Pt_1Zn_1, 1:1 intermetallic alloy phase (red line) with a tetragonal AuCu structure. No additional PtZn alloy phases (i.e., Pt_3Zn, Pt_3Zn_{10}, $PtZn_{1.7}$) were observed on the $PtZn/SiO_2$ catalyst, thereby indicating that the high symmetry Pt_1Zn_1 alloy was preferentially formed. Figure 2c shows a structural comparison between the Pt (fcc) and Pt_1Zn_1 (tetragonal AuCu) phases along with a comparison of the Pt−Pt and Pt−Zn bond distances as determined by EXAFS fittings and from the diffraction peaks below 6° in the XRD patterns of the reduced samples at room temperature. The Pt−Pt and Pt−Zn bond distances derived from in situ XRD and EXAFS are quite similar except for a small systematic error of ∼0.02 Å between the two techniques that has been observed by others.[34] A complete list of Pt and Pt_1Zn_1 unit cell parameters can be found in Table S3.

The diffraction pattern of $PtZn/SiO_2$ collected at room temperature upon exposure to air after reduction at 600 °C exhibited features in addition to those for the PtZn intermetallic alloy, likely due to surface alloy decomposition induced by exposure to oxygen (Figure S7). The difference pattern (black line) obtained by subtraction of the room temperature oxidized $PtZn/SiO_2$ from reduced $PtZn/SiO_2$ is shown in Figure 3. The peaks in the difference pattern correspond to Pt_1Zn_1 and show that the alloy surface structure was identical to that of the fully reduced Pt_1Zn_1 intermetallic nanoparticle. This Pt_1Zn_1 intermetallic structure on the nanoparticle surface isolated all the surface Pt sites and thereby contributed to the high alkane dehydrogenation selectivity. This relation is consistent with previous observations for SiO_2-supported PdZn,[19,20] PdIn,[21] and PtIn[22] catalysts.

Experimental and Calculated RIXS Planes for Pt and PtZn. Energy differences between the unoccupied and occupied Pt 5d states (i.e., the energy transfer, ΔE, see Scheme 1) for reduced Pt/SiO_2 and $PtZn/SiO_2$ catalysts were examined with *in situ* RIXS by monitoring the Pt L_3 X-ray absorption and emission. The X-ray emission intensity was measured as a function of the incident and emitted photon energies for the Pt

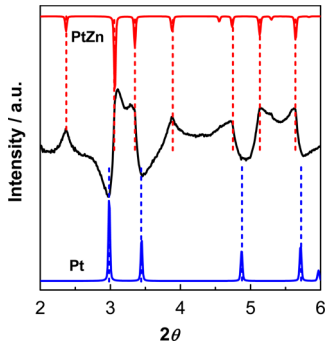

Figure 3. *In situ* XRD patterns for the PtZn surface layer on $PtZn/SiO_2$. Comparison of simulated XRD patterns for Pt (blue line) and Pt_1Zn_1 (red line) with experimentally obtained difference pattern for 9.53 wt % Pt−9.28 wt % Zn/SiO_2 (black line).

L_3 XANES and $L\beta_5$ regions, respectively. The experimentally measured RIXS spectra for Pt/SiO_2 and $PtZn/SiO_2$ are presented in Figure 4 as two-dimensional contour plots that show the energy transfer (ΔE) as a function of the incident photon energy (Ω). For Pt/SiO_2, the maximum RIXS intensity (red region) occurred at Ω = 11 564 eV with an energy transfer of 4.0 eV. Addition of Zn to Pt/SiO_2 shifted the maximum RIXS intensity to higher energy transfer by approximately 2.0 eV at 11 566 eV ($\Delta E \sim 6$ eV), with a high intensity tail that extended along the diagonal to 11 572 eV. A comparison of Pt L_3 XANES in Figure S5 for Pt and PtZn indicates that the edge energy of the latter was shifted to 0.9 eV higher than that in the former. Since the energy transfer for Pt_1Zn_1 was 2.0 eV, the energy of the filled valence states was 1.1 eV lower for Pt_1Zn_1 than that in the monometallic Pt sample. The longer tail in the energy transfer plot for Pt_1Zn_1 (Figure 4) is, in part, due to the broader XANES spectrum of PtZn compared to that of Pt (Figure S5).

Simulations of *in situ* RIXS spectra for Pt and PtZn were performed on Pt(111) and Pt_1Zn_1(110) surfaces and are also shown in Figure 4. The (111) and (110) close-packed surface orientations were chosen in order to represent the bulk nanoparticle surface structures of Pt and Pt_1Zn_1, respectively. Calculated bulk and surface d-DOS were averaged for Pt(111) and Pt_1Zn_1(110) in order to approximate the Pt and Pt_1Zn_1 nanoparticles, respectively. The formalism for calculating RIXS spectra from the DOS has been discussed elsewhere.[24,35,36] RIXS intensities (F) were calculated from the following equation:[24]

$$F(\Omega, \omega) = \int_{\varepsilon_j}^{\varepsilon_i} d\varepsilon \frac{\rho_d(\varepsilon)\,\rho_d'(\varepsilon + \Omega - \omega)}{(\varepsilon - \omega)^2 + \frac{\Gamma_n^2}{4}} \quad (1)$$

Here, F was calculated by integrating over the DOS energies (ε) for the occupied valence states (i) and unoccupied valence states (j), where ρ_d and ρ_d' are the partial d-band DOS of Pt for the occupied and unoccupied states, respectively. The lifetime broadening of the $2p_{3/2}$ core hole (Γ_n) was taken as 5.41 eV.[24] This method does not account for interactions from the photoexcitation process; however, it has been shown to give accurate results when compared to experimental results.[24] The calculations, which were performed by using the d-band DOS obtained through self-consistent DFT calculations, exhibited similar features to the experimental spectra. In particular, the simulations revealed a ∼1.8 eV increase in the energy transfer

DOI: 10.1021/acscatal.6b03603
ACS Catal. 2017, 7, 4173−4181

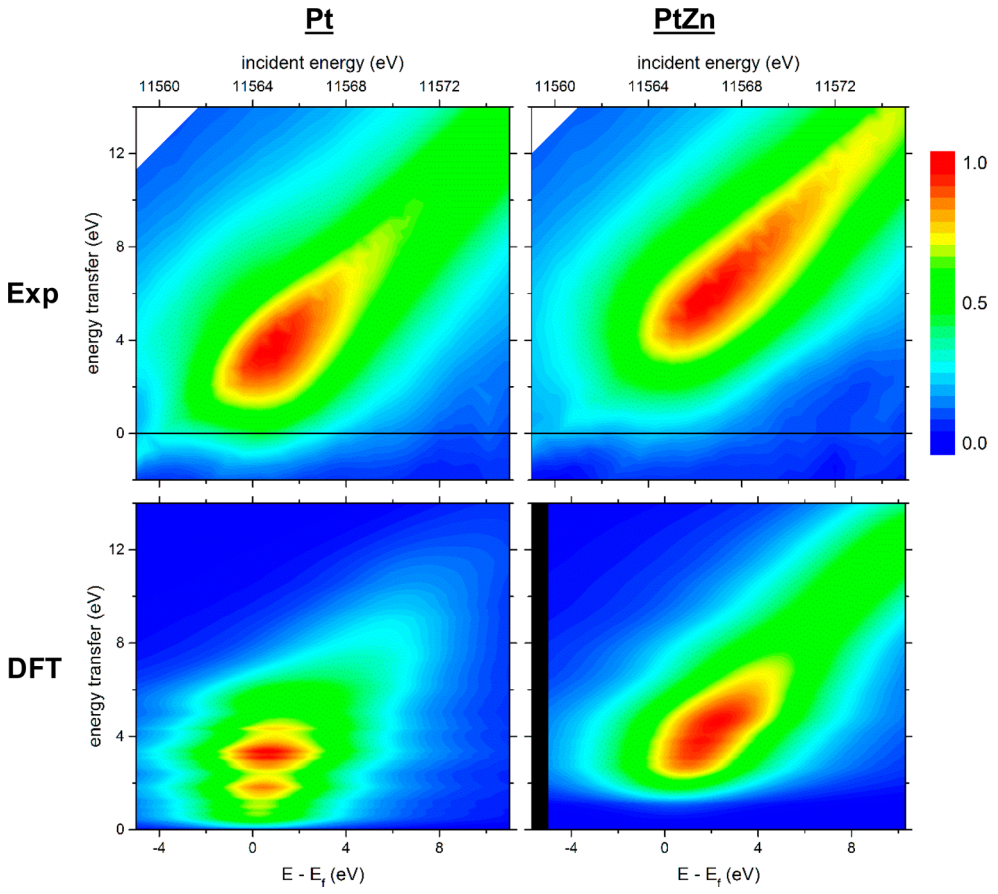

Figure 4. RIXS planes for supported Pt and PtZn nanoparticles. Comparisons between experimentally (Exp) measured RIXS for 9.70 wt % Pt/SiO_2 with calculated RIXS for Pt(111) by DFT (left column), and experimental RIXS for 9.53 wt % Pt−9.28 wt % Zn/SiO_2 with calculated RIXS for Pt_1Zn_1(110) by DFT (right column).

of the RIXS maximum that occurred at ∼0.9 eV higher incident energy than on Pt(111), in agreement with the measured 0.9 eV edge energy increase for PtZn/SiO_2 from *in situ* XAS.

Previous theoretical studies have provided strong evidence that the metal d-band center is a useful descriptor of catalytic activity for various transition metals and alloys.[6,7,37−40] For the present study, the calculated Pt d-band center for monometallic Pt(111) was found to be −2.19 eV and was shifted upward to −2.08 eV for Pt_1Zn_1(110), as shown in Figure 5. Use of a modified electronic structure descriptor,[41] defined as the sum of the d-band center and half the d-DOS width, yielded values of −0.64 eV and −0.61 eV for Pt and Pt_1Zn_1, respectively. Such small changes are within the uncertainty of DFT calculations and do not differentiate the electronic properties in these samples. Indeed, when compared to the experimentally measured RIXS spectra in Figure 4, it is evident that the calculated $L\beta_5$ RIXS planes for Pt(111) and Pt_1Zn_1(110), which contain information corresponding to the surface d-band DOS that affects catalytic activity, accurately reproduce trends in the PtZn and Pt RIXS signatures and provide additional details regarding the Pt valence electronic structure, including a more direct comparison between theoretical and experimental spectra for Pt and PtZn compared to the d-band model alone.

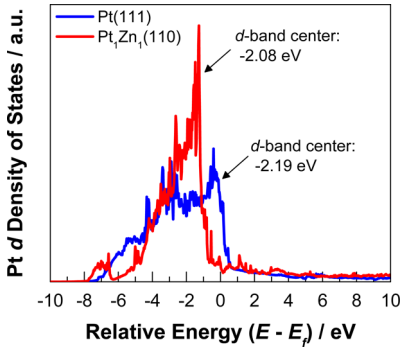

Figure 5. Projected density of states (DOS) for d orbitals of Pt(111) and Pt_1Zn_1(110). The vertical axis represents the electron density, and the horizontal axis corresponds to the energy relative to the Fermi energy (E_f).

The effect of Zn addition on the energy levels of both the occupied and unoccupied Pt 5d bands, evaluated from the energy transfer (ΔE) and Pt L_3 edge energy obtained during *in situ* RIXS and XANES, respectively, is shown in Scheme 2. Compared to monometallic Pt, the occupied Pt 5d bands in PtZn were shifted by approximately 1.1 eV further below the Fermi energy, while the unoccupied bands were shifted to higher energies by approximately 0.9 eV. As discussed in section 4 of the Supporting Information, the lower energies of the occupied states led to an upward shift in the high intensity peak for the Pt_1Zn_1 alloy compared to monometallic Pt, while the extended unoccupied states led to a longer tail for PtZn compared to Pt. This combination of lower energy for the filled and higher energy for the unfilled electronic states changes the relative energy between the Pt d orbitals in PtZn/SiO_2 and the

DOI: 10.1021/acscatal.6b03603
ACS Catal. 2017, 7, 4173−4181

Scheme 2. Energy Level Diagram for Pt 5d Valence Bands in Pt/SiO_2 and Pt_1Zn_1/SiO_2

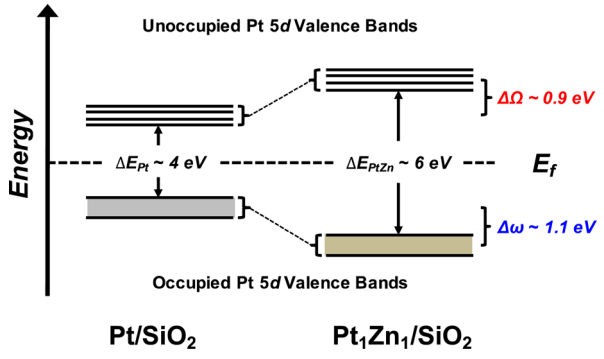

adsorbate electrons, which decreases the Pt-adsorbate bond energy and increases the number of reaction turnovers per Pt site per unit time. Previous microcalorimetric and DFT studies by Dumesic and co-workers[11−13] have shown that the addition of Zn and Sn ad-metals to Pt- and Pd-containing catalysts weakened the interaction of the metal surface with C_2H_4 to inhibit production of coke-forming ethylidyne species. These findings align with the kinetic and structural characterization results from the present study that show suppressed coke deposition and TOR enhancement on the Pt_1Zn_1 nanoparticle alloys. Furthermore, DFT calculations and *in situ* RIXS measurements indicate that the mechanism of this electronic promotion of Pt by Zn for EDH is driven by changes in energy of the Pt 5d electrons, rather than a change in electron occupancy due to electron donation as previously suggested for PtZn[8,10] and PtCu,[40] which effectively reduces the binding energies of adsorbates and increases the TOR per surface Pt.

A major challenge in the development of catalytic materials is the ability to identify the most important properties of a solid surface which govern its chemical reactivity. The molecular level insight obtained in the present study provides a model to suggest that control of the geometric structure of the Pt active sites affects product selectivity, while control of the metal promoter affects the adsorbate binding strength and TOR. Furthermore, the direct experimental validation of DFT-predicted RIXS planes for Pt/SiO_2 and $PtZn/SiO_2$ enables new opportunities to investigate relationships between the energy levels of filled and unfilled valence states for various Pt-containing alloys, the binding energies of adsorbates, and their effects on catalytic activity for EDH. While only monometallic Pt and the Pt_1Zn_1 alloy have been considered here for EDH, we envision that this approach could be applied to other nanoparticle alloys and reactions of interest.

CONCLUSIONS

The combined theoretical and experimental approach for EDH on Pt/SiO_2 and $PtZn/SiO_2$ demonstrates that the addition of Zn to Pt effectively suppresses C−C bond cleavage pathways during dehydrogenation at 600 °C to achieve nearly 100% C_2H_4 selectivity up to the thermodynamic limit of C_2H_6 conversion. Additionally, Zn incorporation into the Pt nanoparticles leads to a 6-fold TOR increase per mole of surface Pt compared to the monometallic Pt catalyst.

Geometric and electronic characterization reveals that the Pt active sites on the surface of the metallic nanoparticles in these catalysts are both structurally and chemically different. The role of the Zn promoter is 2-fold: (i) to form a Pt_1Zn_1 intermetallic alloy structure with uniformly isolated Pt surface sites that effectively suppress the rate of structure-sensitive reactions, such as hydrogenolysis and cracking, while retaining the structure-insensitive dehydrogenation pathway, and (ii) to lower the energy of the filled states of the Pt surface, thus weakening the bond formation between the 5d orbitals and adsorbates. While the selectivity changes may be explained by an ensemble effect related to isolated Pt sites, the TOR enhancement implies an electronic change within the individual Pt atoms, as evidenced by differences in apparent activation energies along with an increase in the Pt RIXS ΔE for $PtZn/SiO_2$ compared to the monometallic Pt/SiO_2 sample. The agreement between experimental and theoretical energies of the Pt 5d valence orbitals for the Pt and Pt_1Zn_1 nanoparticles in this application demonstrates that DFT calculations provide accurate simulations of the RIXS spectra, yielding insights into the electronic structural details and reactivity of these metal surfaces while also supplementing existing studies based on the first moment of the d-band.

EXPERIMENTAL SECTION

Catalyst Synthesis. *Pt/SiO_2.* The incipient wetness impregnation (IWI) method was used with 5 g of commercially available high-purity SiO_2 (Davisil grade 636, 480 m^2 g^{-1}) and an aqueous solution of 0.8 g of $(NH_3)_4Pt(NO_3)_2$ (Sigma-Aldrich) in 5 mL of deionized water for ∼5 wt % Pt loading. The precatalyst was dried in an oven at 100 °C for 24 h, followed by a second impregnation of 0.8 g of $(NH_3)_4Pt(NO_3)_2$ in 5 mL of deionized water to obtain 9.70 wt % Pt loading, as measured by elemental analysis (Galbraith Laboratories). The sample was dried a second time at 100 °C for 24 h and then calcined in air at 225 °C for 3 h. After cooling to room temperature (RT), the sample was reduced in 25% H_2 and balance He according to the following temperature cycle: (i) ramp from RT to 100 °C at 5 °C min^{-1}, hold at 100 °C for 15 min; (ii) ramp to 150 °C at 5 °C min^{-1}, hold at 150 °C for 15 min; (iii) ramp to 200 °C at 2.5 °C min^{-1}, hold at 200 °C for 30 min; (iv) ramp to 225 °C at 2.5 °C min^{-1}, hold at 225 °C for 30 min; (v) ramp to 300 °C at 2.5 °C min^{-1}, hold at 300 °C for 15 min; (vi) ramp to 600 °C at 5 °C min^{-1}, hold at 600 °C for 15 min; (vii) purge with He at 600 °C for 15 min and cool to RT in He.

$PtZn/SiO_2$. An aqueous solution of $Zn(NO_3)_2$ was prepared by dissolving 1.8 g of $Zn(NO_3)_2{\cdot}6H_2O$ (Sigma-Aldrich) into 3 mL of deionized water and adjusting the pH to 11 with 2 mL concentrated NH_4OH. Deionized water was added to raise the solution volume to 10 mL. IWI was used with 5 g of high-purity SiO_2 (Davisil grade 636, 480 m^2 g^{-1}) and the $Zn(NO_3)_2$ solution to obtain ∼5 wt % Zn loading. The precatalyst was dried in an oven at 100 °C for 24 h, followed by a second impregnation of $Zn(NO_3)_2$ solution (pH adjusted to 11) to obtain 9.28 wt % Zn loading. The sample was dried a second time at 100 °C for 24 h and then calcined in air at 550 °C for 3 h followed by annealing in He at 600 °C for 15 min. After cooling to RT, the 10 wt % Zn/SiO_2 sample was twice impregnated with aqueous solutions of 0.8 g of $(NH_3)_4Pt(NO_3)_2$ (Sigma-Aldrich) in 5 mL of deionized water to obtain 9.53 wt % Pt loading. The final Zn and Pt loadings were measured by elemental analysis (Galbraith Laboratories). The 9.53 wt % Pt−9.28 wt % Zn/SiO_2 precatalyst was calcined in air at 225 °C and reduced in 25% H_2 and balance He per the same procedure as the 9.70 wt % Pt/SiO_2 catalyst.

DOI: 10.1021/acscatal.6b03603
ACS Catal. 2017, 7, 4173−4181

Kinetic Measurements. Catalyst testing was performed in a quartz, plug-flow reactor (9.5 mm I.D.) with a U-shaped effluent line. The catalyst section has a well for a K-type thermocouple (3.2 mm O.D.) for temperature indication that is contained within a quartz sheath and placed in the bottom center of the catalyst bed to measure the reaction temperature inside of the bed. A furnace connected to a temperature controller is used to supply heat to the reactor and maintain the reaction at the desired temperature. The mass of the catalyst sample ranged from 0.01 to 0.2 g, depending upon the desired conversion. The catalyst was diluted with high-purity SiO_2 (Davisil grade 636, 480 m^2 g^{-1}) to maintain the catalyst bed height at ~12.7 mm (1/2 in.).

The reactor gas delivery system consists of five mass flow controllers (2-Brooks 5850E, 2-Porter 201, 1-Tylan FC-260) and a manifold that mixes the gases prior to entering the reactor. First, the catalyst was reduced in 5% H_2 (Praxair, 99.999%) and balance N_2 (Matheson, 99.995%) at 40 mL min^{-1} total flow while the temperature was ramped from RT to 600 °C at 10 °C min^{-1} and then held at 600 °C for 30 min. The total flow rate was confirmed at the reactor outlet. Then, following the reduction, the EDH reaction mixture was introduced into the reactor at 600 °C and 150 mL min^{-1} total flow. The EDH reaction mixture consists of 2.5% C_2H_6 (Matheson, 99.95%), 1% H_2 (Praxair, 99.999%), 0.5% C_2H_4 (Matheson, 99.999%), 46.7% He (Matheson, 99.999%), and balance N_2 (Matheson, 99.995%), which was used as an internal standard. The reactor effluent was analyzed by using a Hewlett-Packard 5890 Series II gas chromatograph (GC) equipped with a thermal conductivity detector (TCD). A Carboxen-1010 PLOT Capillary GC Column was used to separate the components in the reactor effluent gas mixture. After the C_2H_6 conversion stabilized below 10% at 600 °C, the apparent activation energy (E_{app}) was measured between 570 and 600 °C. Details regarding the calculation of EDH rates, ethane conversion, and ethylene selectivity can be found in section 3 of the Supporting Information. During each run, carbon mass balances closed from 83 to 100% for Pt/SiO_2 (with C_2H_4 cofed), 95 to 100% for Pt/SiO_2 (without C_2H_4 cofed), and ~100% for $PtZn/SiO_2$ both with and without C_2H_4 cofed.

X-ray Characterization. *X-ray Absorption.* Platinum L_3 (11 564 eV) XAS experiments were performed in transmission mode at the Materials Research Collaborative Access Team (MRCAT) bending magnet (10-BM) beamline at the Advanced Photon Source (APS) within Argonne National Laboratory to identify the Pt chemical state, coordination (N), types of nearest neighbors, and interatomic bond distances (R). A cylindrical sample holder containing six wells to hold self-supporting catalyst wafers was placed inside of a quartz tube (25.4 mm O.D.) and sealed with Kapton windows and Ultra-Torr fittings to allow gases to flow through the cell. The thickness of the catalyst wafers (~15 mg) was chosen to give an X-ray absorbance of approximately 2.0 and a Pt edge step of approximately 0.5. After reduction at 600 °C in 3% H_2 and balance He, the Pt/SiO_2 and $PtZn/SiO_2$ samples were cooled to room temperature in H_2, and then X-ray absorption spectra were collected by using standard methods and energy calibrated to the simultaneously obtained edge position of a Pt foil. The Pt edge energy was determined on the basis of the position of the maximum of the first peak in the first derivative of the XANES region. Phase shifts and backscattering amplitudes for the EXAFS spectra were determined for monometallic Pt scatterers (i.e., Pt−Pt) based on the experimentally obtained Pt foil spectra (12 scatterers at 2.77 Å). Pt−Zn scatterers were calculated by using two atom calculations with the FEFF6 code.[42,43] X-ray absorption spectra were analyzed with WinXAS v. 3.11 software.[44] The values for the amplitude reduction factor, S_0^2, and Debye−Waller factor (DWF), $\Delta\sigma^2$, were determined by fitting the foils with FEFF. The EXAFS parameters were calculated for the first scattering shell by using the FEFF references and performing a least-squares fit in R-space of the k^2-weighted Fourier transform. Once the nanoparticle structure was determined by XRD, the final EXAFS fit was performed by using Artemus software[45] based on a two shell fit (i.e., Pt−Zn and Pt−Pt) of the Pt_1Zn_1 structure.

Synchrotron X-ray Diffraction. XRD measurements were performed in transmission mode at the Sector 11 insertion device (11-ID-C) beamline at the APS. XRD patterns were acquired by using X-rays at 105 keV (λ = 0.11798 Å) and a PerkinElmer large area detector with a typical exposure time of 5 s and a total of 30 scans. Catalyst samples were pressed into cylindrical, self-supporting wafers (d ~ 7 mm) and placed on a Pt crucible inside of a ceramic sample cup within a Linkam Scientific TS1500 heating stage. The heating stage is equipped with water cooling and allows for temperature-controlled operation while flowing gases across the catalyst wafer. The 2-D scattering images were converted to 1-D scattering patterns by using Fit2D software in order to obtain plots of intensity as a function of 2θ.[46] Materials Analysis Using Diffraction (MAUD) v. 2.55 software was used to simulate standard XRD patterns of Pt,[47] Pt_1Zn_1,[48] Pt_3Zn,[49] Pt_3Zn_{10},[50] and $PtZn_{1.7}$[49] phases. These simulated patterns were then compared with the experimentally measured patterns for 10 wt % Pt/SiO_2 and 10 wt % $PtZn/SiO_2$.

Resonant Inelastic X-ray Scattering. RIXS measurements were obtained on the MRCAT insertion device (10-ID) beamline at the APS. Catalyst samples (~50−75 mg) were pressed into self-supporting wafers at a 45° angle and placed inside of a custom *in situ* gas cell that is equipped with a resistively heated sample stage, water-cooled Kapton windows, dual thermocouples for temperature indication and control, and connections to allow gases to flow through the cell.[51] The catalysts were reduced in 3% H_2 and balance He (50 mL min^{-1} total flow) at 550 °C for 0.5 h and then cooled to 100 °C in the same gas mixture prior to analysis.

The X-ray emission spectrometer was based on a bent silicon Laue analyzer,[52] optimized for high resolution. Soller slits were used for background suppression, and a Pilatus 100 K pixel area detector (Dectris Ltd.) was used to detect the X-rays. The silicon analyzer element was a 55-μm-thick wafer, with <100> orientation, cylindrically bent to a minimum radius of 480 mm (as a logarithmic spiral). The (133) reflection with a calculated asymmetry of 13.26° was used to select the pass band. The calculated reflectivity, absorption, and local bandwidth at 11 560 eV were 53%, 30%, and 1.1 eV, respectively. Soller slits absorbed unreflected X-rays and reduced the background scatter. To generate the RIXS planes, the incident X-ray energy was scanned from 11 547 eV to 11 589 eV in 0.7 eV steps above 11 558 eV. The entire emission energy range was measured at once by carefully setting the analyzer angle and distance from the sample. Once set, the analyzer remained fixed during the measurement. Each pixel of the array detector then must be assigned an energy. Resonant valence emission has a complication for energy calibration in that the elastic scatter

DOI: 10.1021/acscatal.6b03603
ACS Catal. 2017, 7, 4173−4181

and the X-ray emission are at nearly the same energy over a portion of the spectrum. Postprocessing of the images was required to generate energy masks for the entire array detector surface. These masks were used to convert the images into intensity versus X-ray energy. To balance the intensity of the elastically scattered X-rays used for calibration with the low background required to observe the X-ray emission, the center of the analyzer was offset by 10° elevation from the plane of the X-ray beam polarization, while being set at 90° in the plan view of the beam, sample, and analyzer. The combined energy resolution of the source, beam size, and analyzer was measured to be about 2.4 eV: comparable to the calculated resolution (2.1 eV) and as well as the valence emission line width.

DFT Methods. All calculations were performed by using self-consistent, periodic density functional theory (DFT), as implemented within the Vienna ab Initio Simulation Package (VASP).[53−56] The Perdew−Burke−Ernzerhof exchange-correlation functional was used for all calculations.[57] The projector augmented wave (PAW) core potentials developed from PBE calculations were used.[58,59] For the Pt and PtZn bulk lattice optimizations, a cutoff energy of 600 eV and a 20 × 20 × 20 Monkhorst−Pack K-point grid with Methfessel-Paxton smearing was used to reduce Pulay stress. Lattice constants are converged to within a force criterion of 0.02 eV $Å^{-1}$, which resulted in lattice parameters of 3.98 Å for Pt and 2.88 and 3.53 Å for the *a* and *c* unit vectors, respectively, of Pt_1Zn_1. For DOS calculations on the Pt and Pt_1Zn_1 bulk, a cutoff energy of 1000 eV and a 30 × 30 × 30 Monkhorst−Pack K-point grid was implemented along with tetrahedron Blöchl smearing. The projected density of state (PDOS) was lm-decomposed according to the Wigner−Seitz radius provided by the PAW potential. Close packed surfaces corresponding to the (111) for Pt as well as the (110) and (101) surfaces for Pt_1Zn_1 were cut from the lattice optimized bulk. Each surface was a five layer slab with a 10 Å vacuum. Cell dimensions for the Pt surface were 5.62 Å, 5.62 Å, and 29.18 Å along the *a*, *b*, and *c* unit vectors, respectively, including vacuum. Cell dimensions for the Pt_1Zn_1(110) surface were 4.08 Å, 3.53 Å, and 28.16 Å along the *a*, *b*, and *c* unit vectors, respectively, including vacuum. Cell dimensions for the PtZn(101) surface were 4.58 Å, 2.88 Å, and 28.93 Å. A comparison of the predicted RIXS planes for the (110) and (101) surfaces is included in section 4 of the Supporting Information. The bottom two layers were fully constrained, and the rest of the slab was allowed to relax to a force criterion of 0.02 eV $Å^{-1}$. An energy cutoff of 400 eV, a 6 × 6 × 1 Monkhorst−Pack K-point grid, and Methfessel-Paxton smearing was found to minimize Pulay stress and converge total energies. DOS calculations were performed with a 1000 eV cutoff energy, an 8 × 8 × 1 Monkhorst−Pack K-point grid, and tetrahedron Blöchl smearing by using the relaxed surface geometries.

■ ASSOCIATED CONTENT

Supporting Information

This material is available free of charge on the ACS Publications Web site at The Supporting Information is available free of charge on the ACS Publications website at DOI: 10.1021/acscatal.6b03603.

Arrhenius plots, HAADF-STEM and TEM images of Pt/SiO_2 and PtZn/SiO_2, Pt and Pt_1Zn_1 metal cluster size distributions, Pt L_3 XANES spectra, *in situ* XRD patterns, Pt_1Zn_1 RIXS energy maps, Pt_1Zn_1 d-DOS, simulated RIXS spectra, hydrogen uptake, Pt L_3 EXAFS fitting parameters, Pt and Pt_1Zn_1 unit cell parameters, kinetic measurement details, DFT calculation details, and associated references (PDF)

■ AUTHOR INFORMATION

Corresponding Authors

*E-mail: jgreeley@purdue.edu.
*E-mail: mill1194@purdue.edu.

ORCID

Viktor J. Cybulskis: 0000-0003-3678-6562
Jeffrey Greeley: 0000-0001-8469-1715

Author Contributions

The manuscript was written through contributions of all authors. All authors have given approval to the final version of the manuscript.

Funding

Qatar National Research Fund No. 13121024 National Science Foundation CBET1437219

Notes

The authors declare no competing financial interest.

■ ACKNOWLEDGMENTS

Use of the Advanced Photon Source is supported by the U.S. Department of Energy, Office of Science, and Office of Basic Energy Sciences, under Contract DE-AC02-06CH11357. MRCAT operations are supported by the Department of Energy and the MRCAT member institutions. We also acknowledge the use of beamline 11-ID-C at the Advanced Photon Source. Support for V.J.C. and H.-T.T. was provided by Qatar National Research Fund No. 13121024. J.G. and B.C.B. acknowledge support from the DMREF program of the National Science Foundation (CBET1437219). We would like to thank Chang Wan Han and Volkan Ortalan in the School of Materials Engineering at Purdue University for providing the STEM and TEM images.

■ REFERENCES

(1) Siirola, J. J. *AIChE J.* **2014**, *60*, 810−819.
(2) Sattler, J. J. H. B.; Ruiz-Martinez, J.; Santillan-Jimenez, E.; Weckhuysen, B. M. *Chem. Rev.* **2014**, *114*, 10613−10653.
(3) Bhan, A.; Nicholas Delgass, W. *Catal. Rev.: Sci. Eng.* **2008**, *50*, 19−151.
(4) Sattler, J. J. H. B.; Gonzalez-Jimenez, I. D.; Luo, L.; Stears, B. A.; Malek, A.; Barton, D. G.; Kilos, B. A.; Kaminsky, M. P.; Verhoeven, T.; Koers, E. J.; Baldus, M.; Weckhuysen, B. M. *Angew. Chem., Int. Ed.* **2014**, *53*, 9251−9256.
(5) Biscardi, J. A.; Iglesia, E. *Catal. Today* **1996**, *31*, 207−231.
(6) Hammer, B.; Nørskov, J. K. *Adv. Catal.* **2000**, *45*, 71−129.
(7) Hammer, B.; Nørskov, J. K. *Surf. Sci.* **1995**, *343*, 211−220.
(8) Yu, Z.; Sawada, J. A.; An, W.; Kuznicki, S. M. *AIChE J.* **2015**, *61*, 4367−4376.
(9) Andy, P.; Davis, M. E. *Ind. Eng. Chem. Res.* **2004**, *43*, 2922−2928.
(10) Yu, C. L.; Xu, H. Y.; Ge, Q. J.; Li, W. Z. *J. Mol. Catal. A: Chem.* **2007**, *266*, 80−87.
(11) Hill, J. M.; Shen, J. Y.; Watwe, R. M.; Dumesic, J. A. *Langmuir* **2000**, *16*, 2213−2219.
(12) Shen, J. Y.; Hill, J. M.; Watwe, R. M.; Spiewak, B. E.; Dumesic, J. A. *J. Phys. Chem. B* **1999**, *103*, 3923−3934.
(13) Silvestre-Albero, J.; Sanchez-Castillo, M. A.; He, R.; Sepulveda-Escribano, A.; Rodriguez-Reinoso, F.; Dumesic, J. A. *Catal. Lett.* **2001**, *74*, 17−25.
(14) Boudart, M.; Djega-Mariadassou, G. Structure-Insensitive and Structure-Sensitive Reactions on Metals. In *Kinetics of Heterogeneous*

DOI: 10.1021/acscatal.6b03603
ACS Catal. 2017, 7, 4173−4181

Catalytic Reactions, 1 ed.; Princeton University Press: Princeton, NJ, 1984; pp 155−193.
(15) Yang, M.-L.; Zhu, Y.-A.; Fan, C.; Sui, Z.-J.; Chen, D.; Zhou, X.-G. *Phys. Chem. Chem. Phys.* **2011**, *13*, 3257−3267.
(16) Virnovskaia, A.; Rytter, E.; Olsbye, U. *Ind. Eng. Chem. Res.* **2008**, *47*, 7167−7177.
(17) Galvita, V.; Siddiqi, G.; Sun, P.; Bell, A. T. *J. Catal.* **2010**, *271*, 209−219.
(18) Yagasaki, E.; Masel, R. I. *Surf. Sci.* **1989**, *222*, 430−450.
(19) Childers, D. J.; Schweitzer, N. M.; Shahari, S. M. K.; Rioux, R. M.; Miller, J. T.; Meyer, R. J. *J. Catal.* **2014**, *318*, 75−84.
(20) Gallagher, J. R.; Childers, D. J.; Zhao, H. Y.; Winans, R. E.; Meyer, R. J.; Miller, J. T. *Phys. Chem. Chem. Phys.* **2015**, *17*, 28144−28153.
(21) Wu, Z.; Wegener, E. C.; Tseng, H. T.; Gallagher, J. R.; Harris, J. W.; Diaz, R. E.; Ren, Y.; Ribeiro, F. H.; Miller, J. T. *Catal. Sci. Technol.* **2016**, *6*, 6965−6976.
(22) Wegener, E. C.; Wu, Z.; Tseng, H.-T.; Gallagher, J. R.; Ren, Y.; Diaz, R. E.; Ribeiro, F. H.; Miller, J. T. *Catal. Today* **2017**, DOI: 10.1016/j.cattod.2017.03.054c. Published Online: April 15, 2017. http://www.sciencedirect.com/science/article/pii/S0920586117302067 (accessed May 4, **2017**).
(23) Singh, J.; Lamberti, C.; van Bokhoven, J. A. *Chem. Soc. Rev.* **2010**, *39*, 4754−4766.
(24) Glatzel, P.; Singh, J.; Kvashnina, K. O.; van Bokhoven, J. A. *J. Am. Chem. Soc.* **2010**, *132*, 2555−2557.
(25) Singh, J.; Nelson, R. C.; Vicente, B. C.; Scott, S. L.; van Bokhoven, J. A. *Phys. Chem. Chem. Phys.* **2010**, *12*, 5668−5677.
(26) Pollock, C. J.; DeBeer, S. *Acc. Chem. Res.* **2015**, *48*, 2967−2975.
(27) Meyer, D. A.; Zhang, X. N.; Bergmann, U.; Gaffney, K. J. *J. Chem. Phys.* **2010**, *132*, 134502.
(28) Thomas, R.; Kas, J.; Glatzel, P.; Al Samarai, M.; de Groot, F. M. F.; Alonso Mori, R.; Kavcic, M.; Zitnik, M.; Bucar, K.; Rehr, J. J.; Tromp, M. *J. Phys. Chem. C* **2015**, *119*, 2419−2426.
(29) Glatzel, P.; Yano, J.; Bergmann, U.; Visser, H.; Robblee, J. H.; Gu, W. W.; de Groot, F. M. F.; Cramer, S. P.; Yachandra, V. K. *J. Phys. Chem. Solids* **2005**, *66*, 2163−2167.
(30) Zhou, Y.; Doronkin, D. E.; Chen, M. L.; Wei, S. Q.; Grunwaldt, J. D. *ACS Catal.* **2016**, *6*, 7799−7809.
(31) Kale, M. J.; Christopher, P. *ACS Catal.* **2016**, *6*, 5599−5609.
(32) Lei, Y.; Jelic, J.; Nitsche, L. C.; Meyer, R.; Miller, J. T. *Top. Catal.* **2011**, *54*, 334−348.
(33) Miller, J. T.; Kropf, A. J.; Zha, Y.; Regalbuto, J. R.; Delannoy, L.; Louis, C.; Bus, E.; van Bokhoven, J. A. *J. Catal.* **2006**, *240*, 222−234.
(34) Gallagher, J. R.; Li, T.; Zhao, H.; Liu, J.; Lei, Y.; Zhang, X.; Ren, Y.; Elam, J. W.; Meyer, R. J.; Winans, R. E.; Miller, J. T. *Catal. Sci. Technol.* **2014**, *4*, 3053−3063.
(35) Kotani, A.; Shin, S. *Rev. Mod. Phys.* **2001**, *73*, 203−246.
(36) Jiménez-Mier, J.; van Ek, J.; Ederer, D. L.; Callcott, T. A.; Jia, J. J.; Carlisle, J.; Terminello, L.; Asfaw, A.; Perera, R. C. *Phys. Rev. B: Condens. Matter Mater. Phys.* **1999**, *59*, 2649−2658.
(37) Mavrikakis, M.; Hammer, B.; Nørskov, J. K. *Phys. Rev. Lett.* **1998**, *81*, 2819−2822.
(38) Hammer, B.; Norskov, J. K. *Nature* **1995**, *376*, 238−240.
(39) Hammer, B.; Morikawa, Y.; Nørskov, J. K. *Phys. Rev. Lett.* **1996**, *76*, 2141−2144.
(40) Linke, R.; Schneider, U.; Busse, H.; Becker, C.; Schröder, U.; Castro, G. R.; Wandelt, K. *Surf. Sci.* **1994**, *307*, 407−411.
(41) Vojvodic, A.; Norskov, J. K.; Abild-Pedersen, F. *Top. Catal.* **2014**, *57*, 25−32.
(42) Rehr, J. J.; Albers, R. C.; Zabinsky, S. I. *Phys. Rev. Lett.* **1992**, *69*, 3397−3400.
(43) Rehr, J. J.; Albers, R. C. *Phys. Rev. B: Condens. Matter Mater. Phys.* **1990**, *41*, 8139−8149.
(44) Ressler, T. *J. Synchrotron Radiat.* **1998**, *5*, 118−122.
(45) Ravel, B.; Newville, M. *J. Synchrotron Radiat.* **2005**, *12*, 537−541.
(46) Hammersley, A. P.; Svensson, S. O.; Hanfland, M.; Fitch, A. N.; Hausermann, D. *High Pressure Res.* **1996**, *14*, 235−248.
(47) Hull, A. W. *Phys. Rev.* **1921**, *17*, 571−588.
(48) Nowotny, H.; Bauer, E.; Stempfl, A. *Monatsh. Chem.* **1950**, *81*, 1164−1164.
(49) Nowotny, H.; Bauer, E.; Stempfl, A.; Bittner, H. *Monatsh. Chem.* **1952**, *83*, 221−236.
(50) Johansson, A.; Westman, S. *Acta Chem. Scand.* **1970**, *24*, 3471−3479.
(51) Bolin, T. B.; Wu, T.; Schweitzer, N.; Lobo-Lapidus, R.; Kropf, A. J.; Wang, H.; Hu, Y.; Miller, J. T.; Heald, S. M. *Catal. Today* **2013**, *205*, 141−147.
(52) Kropf, A. J.; Fortner, J. A.; Finch, R. J.; Cunnane, J. C.; Karanfil, C. *Phys. Scr.* **2005**, *T115*, 998−1000.
(53) Kresse, G.; Hafner, J. *Phys. Rev. B: Condens. Matter Mater. Phys.* **1993**, *47*, 558−561.
(54) Kresse, G.; Hafner, J. *Phys. Rev. B: Condens. Matter Mater. Phys.* **1994**, *49*, 14251−14269.
(55) Kresse, G.; Furthmüller, J. *Comput. Mater. Sci.* **1996**, *6*, 15−50.
(56) Kresse, G.; Furthmüller, J. *Phys. Rev. B: Condens. Matter Mater. Phys.* **1996**, *54*, 11169−11186.
(57) Perdew, J. P.; Burke, K.; Ernzerhof, M. *Phys. Rev. Lett.* **1996**, *77*, 3865−3868.
(58) Blöchl, P. E. *Phys. Rev. B: Condens. Matter Mater. Phys.* **1994**, *50*, 17953−17979.
(59) Kresse, G.; Joubert, D. *Phys. Rev. B: Condens. Matter Mater. Phys.* **1999**, *59*, 1758−1775.

DOI: 10.1021/acscatal.6b03603
ACS Catal. 2017, 7, 4173−4181